Maximilian Schenk
Institute of Fluid Mechanics and Heat Transfer,
TU Wien,
Vienna 1060, Austria

Georgios Giamagas
Institute of Fluid Mechanics and Heat Transfer,
TU Wien,
Vienna 1060, Austria;
DPIA,
University of Udine,
Udine 33100, Italy

Alessio Roccon
Institute of Fluid Mechanics and Heat Transfer,
TU Wien,
Vienna 1060, Austria;
DPIA,
University of Udine,
Udine 33100, Italy

Alfredo Soldati
Institute of Fluid Mechanics and Heat Transfer,
TU Wien,
Vienna 1060, Austria;
DPIA,
University of Udine,
Udine 33100, Italy

Francesco Zonta[1]
Institute of Fluid Mechanics and Heat Transfer,
TU Wien,
Vienna 1060, Austria
e-mail: francesco.zonta@tuwien.ac.at

Computationally Efficient and Interface Accurate Dual-Grid Phase-Field Simulation of Turbulent Drop-Laden Flows

In this work, we develop a dual-grid approach for the direct numerical simulations of turbulent multiphase flows in the framework of the phase-field method (PFM). With the dual-grid approach, the solution of the Navier–Stokes equations (flow-field) and of the Cahn–Hilliard equation (phase-field) are performed on two different computational grids. In particular, a base grid—fine enough to resolve the flow down to the Kolmogorov scale—is used for the solution of the Navier–Stokes equations, while a refined grid—required to improve the description of small interfacial structures—is used for the solution of the Cahn–Hilliard equation (phase-field method). The proposed approach is validated, and its computational efficiency is evaluated considering the deformation of a drop in a two-dimensional shear flow. Analyzing the computational time and memory usage, we observe a reduction between $\simeq 30\%$ and $\simeq 40\%$ (with respect to the single-grid approach), depending on the grid refinement factor employed for the phase-field variable. The applicability of the approach to a realistic three-dimensional case is also discussed, by focusing on the breakage of a thin liquid sheet inside a turbulent channel flow. Indications on the grid resolution representing a good compromise between accuracy and computational efficiency in drop-laden turbulence are also provided. [DOI: 10.1115/1.4065504]

1 Introduction

Turbulent flows laden with drops and particles are commonly encountered in a number of natural and industrial processes. Examples include the formation of raindrops in the atmosphere and at the ocean surface [1–3], the atomization and spray generation in fuel injection and combustion [4–6], the transmission of respiratory diseases [7–9] and many other flow instances [10,11].

The key issue in the numerical analysis of turbulent multiphase flows is the wide range of spatial and temporal scales involved in the problem: from flow phenomena that occur within a range of scales between the integral (large) and the Kolmogorov (small) scale, to interfacial phenomena, that occur within a much wider range of scales, from the drop/bubble scale down to the molecular scale of the interface. Typically, the scale separation between flow and interfacial scales is about eight to nine orders of magnitude, a situation which makes accurate simulations—taking into account all flow and interfacial scales—extremely challenging to perform

[12–14]. In addition, the numerical description of an ever-moving and deforming interface requires numerical methods able to capture its deformation and topological changes. We can identify two different macrofamilies of numerical methods: interface tracking methods, where the interface is explicitly tracked with the use of marker points, and interface-capturing methods, where the interface is identified as the isovalue of a color (or marker) function. Because of their flexibility, interface capturing methods (e.g., volume-of-fluid, level-set and phase-field methods [15–17]) are widely used. Yet, in the context of interface capturing methods, it is desirable to solve the color/marker function variable on a grid that is refined as much as possible, so that small drops/bubbles and thin fluid ligaments can be accurately captured and topological changes better described [14,18,19]. Naturally, there is a limit to the grid resolution that can be afforded, even using cutting-edge high-performance computing resources.

The challenge associated with the idea of resolving all the involved length scales of the problem, along with the limitation on the maximum grid resolution that can be used has driven researchers toward the development of different strategies. Two possibilities are available to increase the efficiency of the computational approaches for multiphase flows: adaptive mesh refinements (AMRs) and

dual-grid approaches. Using AMR schemes [20,21], the computational grid is locally refined near the interface, where most of the marker function gradients are located, while a coarser grid (thus reducing the computational cost) can be adopted farther from the interface. This strategy has been applied to the most popular interface capturing methods (using quadtree-, octree-based algorithms), like volume-of-fluid [22–25], level-set [26–32], Lattice-Boltzmann [33,34], and phase-field methods [35,36]. Differently, using dual-grid approaches (or multiresolution strategies), the flow-field is resolved on a base grid, fine enough to capture the smallest flow scale (i.e., order of the Kolmogorov length-scale) while the marker function is solved on a more refined grid so that smaller interfacial features can be described [37–40]. Each of these techniques has its own advantages and disadvantages. On one hand, while in principle AMR schemes provide the most cost-effective strategy (as the grid is only refined at the interface location), it is not straightforward to balance properly the load among the different parallel tasks (i.e., to have an optimum scalability) as the load balance depends on the interface location. In addition, AMR schemes, are mainly suitable for local methods (e. g., finite difference, finite volume, finite-element, or Lattice-Boltzmann methods) and less applicable to global methods, like pseudo-spectral methods [41]. On the other hand, dual-grid approaches are less effective in reducing the computational cost, but are less influenced by scalability issues (as the computational load per parallel process does not vary over time) and can be applied to different numerical methods [37–40]. These differences are also reflected in the ease of implementation of these two techniques. Generally speaking, AMR is of more difficult implementation, and external libraries [31,42] are often used, while the dual-grid approach is easier to implement, as the solution schemes do not require extensive modifications.

In this work, we develop and test a dual-grid approach for the direct numerical simulation of multiphase turbulence. The proposed approach relies on the pseudo-spectral direct numerical simulation of turbulence—used to describe the flow-field—coupled with a phase-field method—used to describe the interface dynamics. We recall here that the phase-field method (PFM) is an interface-capturing method that is based on the introduction of an order parameter, ϕ, which is constant and uniform in the bulk phases ($\phi = \pm 1$), while it undergoes a smooth transition across the interface separating the two phases. As the solution of the Navier–Stokes equations in very fine grids is extremely time- and memory-demanding, we use two different computational grids: a base grid for the flow-field (which must be fine enough to solve for the flow-field down to the Kolmogorov scale), and a refined grid for the phase-field variable. This allows for the accurate description of the flow-field, while at the same time improving the description of the small interfacial features (drops, ligaments). To the best of our knowledge, the dual-grid approach is here applied for the first time to pseudo-spectral simulations of multiphase turbulence.

The paper is organized as follows. First, the governing equations and the numerical method are presented, Secs. 2 and 3. Then, the proposed method is benchmarked for the case of a drop released in a laminar shear flow, Sec. 4, and later used to study the breakage of a thin liquid sheet in turbulence, Sec. 5. Finally, conclusions are drawn, Sec. 6.

2 Methodology

The numerical method that was previously developed to study the dynamics of clean and surfactant-laden interfaces in turbulence [19,43–45], is here extended to allow for the use of a dual-grid approach: a base grid is used to solve for the flow-field, while a finer grid is used to solve for the dynamics of the interface. The reference geometry consists of a plane channel, whose reference length is the half-height, h. In the following, the main features of the proposed approach will be presented and discussed.

2.1 Phase-Field Method. The PFM is an interface-capturing method used for the description of multiphase flows. The method is based on the introduction of a marker function—the phase-field variable ϕ—that is uniform in the bulk of the phases ($\phi = \pm 1$ in the two phases) while it varies smoothly over the thin transition layer that separates the two phases [17,46,47]. The time evolution of the phase-field variable can be described by the Cahn–Hilliard (CH) equation which, in dimensionless form, reads as

$$\frac{\partial \phi}{\partial t} + \mathbf{u} \cdot \nabla \phi = \frac{1}{\text{Pe}} \nabla^2 \mu + f_p \tag{1}$$

where $\mathbf{u} = (u_x, u_y, u_z)$ is the velocity vector, μ is the chemical potential, and f_p is the penalty flux term used in the profile-corrected formulation of the phase-field method, and will be discussed better below. The Péclet number, Pe, represents the ratio between the diffusive timescale, $h^2 / \mathcal{M} \beta^2$, and the convective time scale, h/u_τ

$$\text{Pe} = \frac{u_\tau h}{\mathcal{M} \beta} \tag{2}$$

where $u_\tau = \sqrt{\tau_w / \rho_c}$ is the friction velocity (with τ_w is the wall shear-stress and ρ_c is the density of the carrier fluid), h is the half-channel height, $\mathcal{M}$ is the mobility parameter, and β is a positive constant introduced in the dimensionless procedure.

The chemical potential, μ, is obtained as the variational derivative of the Ginzburg–Landau free-energy functional [17,19,48,49]. To model the case of two immiscible fluids, the free-energy functional, $\mathcal{F}[\phi, \nabla \phi]$, is composed by the sum of two different contributions [17,48]

$$\mathcal{F}[\phi, \nabla \phi] = \int_\Omega (f_0 + f_{\text{mix}}) d\Omega \tag{3}$$

$$f_0 = \frac{1}{4} \left(\phi^2 - 1 \right)^2 \tag{4}$$

$$f_{\text{mix}} = \frac{\text{Ch}^2}{2} |\nabla \phi|^2 \tag{5}$$

The first term, f_0, indicates the tendency for the multiphase system to separate into the two pure stable phases, while the second contribution, f_{mix} (mixing energy), is a nonlocal term accounting for the energy stored at the interface. The Cahn number, $\text{Ch} = \epsilon/h$, represents the dimensionless thickness of the interfacial layer separating the two phases. By taking the functional derivative (with respect to ϕ) of the Ginzburg–Landau free-energy functional, we obtain the expression of the chemical potential

$$\mu = \frac{\delta \mathcal{F}[\phi, \nabla \phi]}{\delta \phi} = \phi^3 - \phi - \text{Ch}^2 \nabla^2 \phi \tag{6}$$

At equilibrium, considering that the chemical potential is constant throughout the domain ($\nabla \mu = \mathbf{0}$), the following (equilibrium) profile is obtained for a planar interface:

$$\phi_{\text{eq}} = \tanh \left(\frac{s}{\sqrt{2}\text{Ch}} \right) \tag{7}$$

where s is the coordinate normal to the interface (located at $s = 0$). From Eq. (7), the characteristic width of the thin interfacial layer (identified as the region where $-0.9 < \phi < 0.9$, Ref. [50]) can be approximated as 4.1Ch. Hence, the width of the transition layer directly depends on the Cahn number, Ch.

Finally, the term f_p in Eq. (1) is a penalty flux that is used to overcome some drawbacks of the original formulation of the method used to solve the CH equation [51–53]. The expression of the penalty flux reads as follows:

$$f_p = \frac{\lambda}{\text{Pe}} \left[\nabla^2 \phi - \frac{1}{\sqrt{2}\text{Ch}} \nabla \cdot \left((1 - \phi^2) \frac{\nabla \phi}{|\nabla \phi|} \right) \right] \tag{8}$$

where λ is a numerical parameter [43,52]. Note that, to converge toward the sharp interface limit, the Péclet number is set equal to Pe = 1/Ch for all simulations [54,55].

2.2 Hydrodynamics. To describe the flow-field of the multiphase system, the Cahn–Hilliard Eq. (1) is coupled with the Navier–Stokes equations [14,56,57]. We consider here two incompressible and Newtonian phases that can have different densities and viscosities. With these assumptions, the Navier–Stokes equations read as

$$\nabla \cdot \mathbf{u} = 0 \qquad (9)$$

$$\rho(\phi)\left(\frac{\partial \mathbf{u}}{\partial t} + \mathbf{u} \cdot \nabla \mathbf{u}\right) = -\nabla p + \frac{1}{\mathrm{Re}_\tau}\nabla \cdot \left[\eta(\phi)(\nabla \mathbf{u} + \nabla \mathbf{u}^\mathrm{T})\right] + \mathbf{f}_\sigma \qquad (10)$$

where p is the pressure-field and $\mathbf{f}_\sigma$ represents the surface tension forces. These forces are here computed using a continuum-surface stress approach as follows [58,59]:

$$\mathbf{f}_\sigma = \frac{3}{\sqrt{8}}\frac{\mathrm{Ch}}{\mathrm{We}}\nabla \cdot [\bar{\tau}_c] \qquad (11)$$

where $\bar{\tau}_c = |\nabla\phi|^2 \mathbf{I} - \nabla\phi \otimes \nabla\phi$ is the Korteweg tensor used to model surface tension forces [60]. The two functions $\rho(\phi)$ and $\eta(\phi)$ are the dimensionless density and viscosity maps [43,61–64]

$$\rho(\phi) = 1 + (\rho_r - 1)\frac{\phi+1}{2}, \quad \text{with} \quad \rho_r = \frac{\rho_d}{\rho_c} \qquad (12)$$

$$\eta(\phi) = 1 + (\eta_r - 1)\frac{\phi+1}{2}, \quad \text{with} \quad \eta_r = \frac{\eta_d}{\eta_c} \qquad (13)$$

where ρ_d and ρ_c (respectively η_d and η_c) are the densities (respectively viscosities) of the drops and carrier phases.

The dimensionless numbers that appear in the Navier–Stokes equation (Eqs. (10) and (11)) are the friction Reynolds number

$$\mathrm{Re}_\tau = \frac{\rho_c u_\tau h}{\eta_c} \qquad (14)$$

which represents the ratio between the inertial and viscous forces, and the Weber number

$$\mathrm{We} = \frac{\rho_c u_\tau^2 h}{\sigma} \qquad (15)$$

which represents the ratio between inertial and surface tension forces (being σ the surface tension). Note that both dimensionless numbers are defined using the carrier phase properties as reference.

2.3 Numerical Method. The Navier–Stokes equations are solved using the wall-normal velocity-vorticity formulation by which they are recast as a set of four equations: (i) a second-order equation for the wall-normal component of the vorticity; (ii) a fourth-order equation for the wall-normal component of the velocity vector; (iii) the continuity equation; and (iv) vorticity definition [65–69]. To obtain the system of governing equations, it is useful to first rewrite the Navier–Stokes equations as follows:

$$\frac{\partial \mathbf{u}}{\partial t} = \mathbf{S} - \nabla p + \frac{1}{\mathrm{Re}_\tau}\nabla^2 \mathbf{u} \qquad (16)$$

where the term $\mathbf{S}$ contains all the nonlinear terms present in the Navier–Stokes equations. By taking the curl of the Navier–Stokes equations, the pressure term vanishes thanks to the identity $\nabla \times \nabla p = 0$ and a transport equation for the vorticity vector is obtained

$$\frac{\partial \boldsymbol{\omega}}{\partial t} = \nabla \times \mathbf{S} + \frac{1}{\mathrm{Re}_\tau}\nabla^2 \omega \qquad (17)$$

By taking again the curl of the vorticity transport equation, the following fourth-order equation for the velocity can be derived:

$$\frac{\partial \nabla^2 \mathbf{u}}{\partial t} = \nabla^2 \mathbf{S} - \nabla(\nabla \cdot \mathbf{S}) + \frac{1}{\mathrm{Re}_\tau}\nabla^4 \mathbf{u} \qquad (18)$$

We solve here for the wall-normal components of the vorticity ω_z and velocity w. Hence, the following equations are solved:

$$\frac{\partial \omega_z}{\partial t} = \frac{\partial S_y}{\partial x} - \frac{\partial S_x}{\partial y} + \frac{1}{\mathrm{Re}_\tau}\nabla^2 \omega_z \qquad (19)$$

$$\frac{\partial(\nabla^2 w)}{\partial t} = \nabla^2 S_z - \frac{\partial}{\partial z}\left(\frac{\partial S_x}{\partial x} + \frac{\partial S_y}{\partial y} + \frac{\partial S_z}{\partial z}\right) + \frac{1}{\mathrm{Re}_\tau}\nabla^4 w \qquad (20)$$

Complemented by the continuity equation and the definition of wall-normal vorticity

$$\omega_z = \frac{\partial v}{\partial x} - \frac{\partial u}{\partial y} \qquad (21)$$

The Cahn–Hilliard equation, which is a fourth-order equation, is split into two second-order equations [48]. In particular, the CH equation is first rewritten in the following way:

$$\frac{\partial \phi}{\partial t} = S_\phi + \frac{s\mathrm{Ch}^2}{\mathrm{Pe}_\phi}\nabla^2 \phi - \frac{\mathrm{Ch}^2}{\mathrm{Pe}_\phi}\nabla^4 \phi \qquad (22)$$

where S_ϕ represents the contribution of the nonlinear terms. The operator splitting $\nabla^2 \phi = \nabla^2 \phi(s\mathrm{Ch}^2 + 1) - s\mathrm{Ch}^2\nabla^2 \phi$ is then applied [48] where the positive coefficient s has been chosen considering the temporal discretization.

The governing equations (9) and (19)–(22) are solved using a pseudo-spectral method: the variables are transformed from the physical into the wavenumber space. In the periodic directions (x and y), all the quantities are expressed by Fourier expansions. In the nonhomogeneous wall-normal direction, they are represented by Chebyshev polynomials. All calculations are carried out in the wavenumber space but the nonlinear terms, which are first computed in the physical space and then transformed back to wavenumber space (pseudo-spectral method). This avoids the evaluation of (computationally expensive) convolutions in the wavenumber space [70,71]. The governing equations are discretized in time using an IMplicit-EXplicit scheme, in which the nonlinear terms are integrated with an Adams–Bashfort scheme, while the linear terms are integrated by a Crank–Nicolson (Navier–Stokes) or by an implicit Euler (Cahn–Hilliard) scheme.

This numerical scheme has been implemented in a parallel Fortran 2003 MPI in-house proprietary code. The parallelization strategy relies on a 2D domain decomposition to divide the workload among all the MPI tasks. The code can also exploit GPU-based high-performance computing infrastructures [72]: the solver execution can be accelerated using openACC directives while the execution of Fourier/Chebyshev transforms can be accelerated exploiting the Nvidia cuFFT libraries. Overall, the computational method adopted allows for the accurate resolution of all the governing equations and the achievement of an excellent parallel efficiency thanks to the fine-grain parallelism of the solver.

Periodic boundary conditions are imposed along the streamwise and spanwise directions (x and y). At the two walls, no-slip boundary conditions are imposed for the velocity, $\mathbf{u}$, while no-flux boundary conditions in the wall-normal direction are imposed for the phase-field, ϕ, and for its second derivative [73]

$$\mathbf{u}(x, y, z/h = \pm 1) = (u_w, 0, 0) \qquad (23)$$
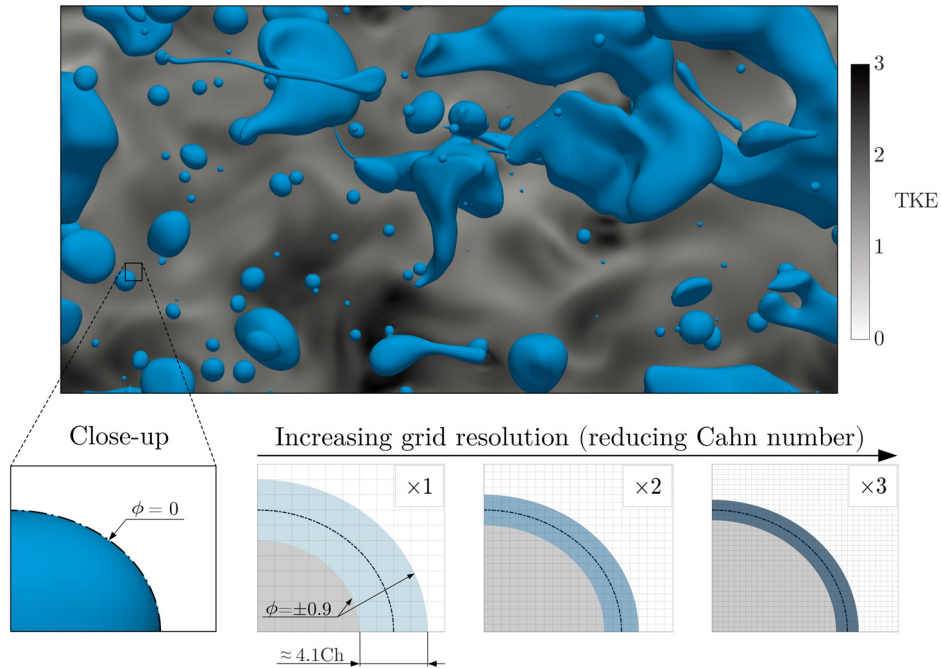
Fig. 1 Three-dimensional rendering of liquid drops in turbulence: drops are visualized by the isocontour $\phi=0$ of the phase-field (panel *a*). The contour shows the turbulent kinetic energy, TKE $= (u_x'^2 + u_y'^2 + u_z'^2)/2$, in a midplane of the channel ($z=0$). Panel *b* shows a close-up view of the rendering where the isolevel $\phi=0$ is explicitly highlighted. In panels *c–e*, we show the effect of increasing the grid resolution (and thus the adoption of smaller Cahn numbers) on the interface representation in the context of the phase-field method for different values of the refinement factor (panel *c* refers to $M_i = 1$; panel *d* refers to $M_i = 2$; panel *e* refers to $M_i = 3$). In particular, a band identifies the region in which the phase-field method undergoes a smooth transition between $\phi=-0.9$ and $\phi=+0.9$. Increasing the grid resolution, smaller Cahn numbers can be adopted and this band narrows around the dot-dashed line ($\phi=0$). Indeed, the characteristic length scale of the thin transition layer is about $\simeq 4.1$Ch. For computational reasons, this layer needs to be discretized with at least three grid points (using a pseudo-spectral method).

$$\frac{\partial \phi}{\partial z}(x, y, z/h = \pm 1) = 0 \qquad (24)$$

$$\frac{\partial^3 \phi}{\partial z^3}(x, y, z/h = \pm 1) = 0 \qquad (25)$$

with u_w is the value prescribed for the streamwise velocity at the wall.

3 Dual-Grid Approach

The key idea of the dual grid approach is the definition of two computational grids: a base reference grid (labeled BG), with $N_x \times N_y \times N_z$ nodes, used to describe the flow-field (which must be fine enough to solve the flow down to the Kolmogorov length-scale), and a finer grid (labeled FG) with $M_x N_x \times M_y N_y \times M_z N_z$ nodes (with M_i positive integer representing the refinement factor along the ith direction) used for the phase-field variable. This strategy is graphically rendered in Fig. 1. Accordingly, time advancement of the solution is achieved by executing, at each time-step, the following substeps:

(i) Velocity field, $\mathbf{u}^n$, is defined and allocated on the BG; phase-field, ϕ^n, is defined and allocated on the FG; variables are transformed in the spectral space, $\hat{\mathbf{u}}^n$ and $\hat{\phi}^n$.
(ii) The surface tension term, which depends on the phase-field variable, is computed on the FG and then, using spectral interpolation, projected onto the BG.
(iii) The nonlinear viscous and inertial terms, which can also depend on the phase-field variable, are computed on the BG.

This operation is accomplished by spectrally interpolating the phase-field variable on the BG.
(iv) Continuity and Navier–Stokes equations are solved (using the wall-normal velocity-vorticity formulation) on the BG to obtain the new velocity field, $\hat{\mathbf{u}}^{n+1}$.
(v) The new velocity field, $\hat{\mathbf{u}}^{n+1}$, is spectrally interpolated onto the FG.
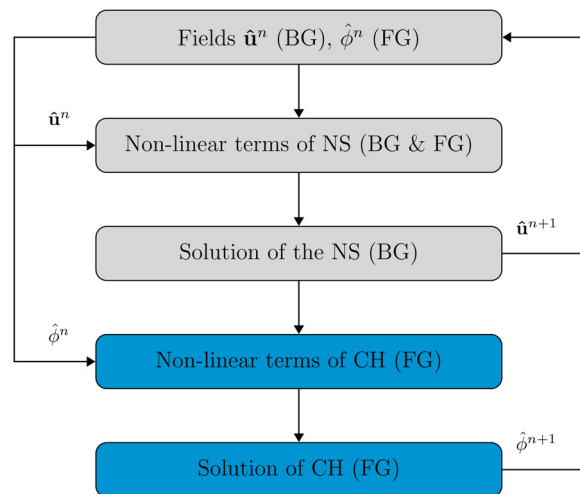

Fig. 2 Flow chart of the substeps required to advance the solution in time from step *n* to step *n* + 1 using the dual-grid approach (BG: base grid and FG: fine grid)
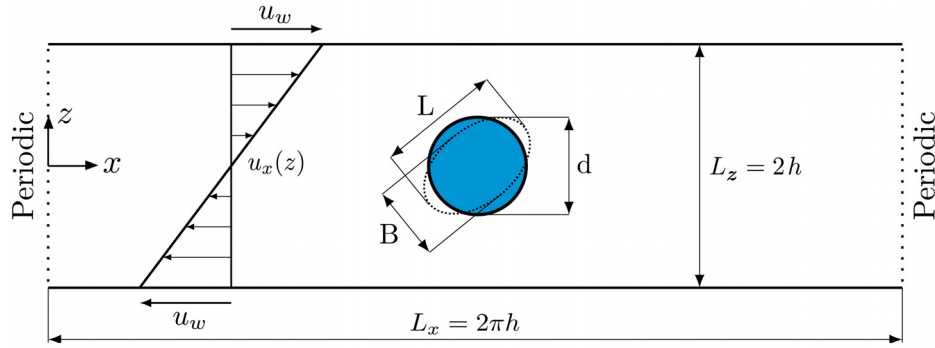
Fig. 3 Sketch of the simulation setup used to study the deformation of a drop in a shear flow. A circular drop of diameter $d = 0.8h$ is located at the center of the channel. The domain is 2D with dimensions $L_x \times L_z = 2\pi h \times 2h$. Periodicity is applied along x, and the two walls move in opposite directions with constant velocity $u_x = u_w = \pm 1$. The imposed shear deforms the drop until a new steady-state configuration is obtained (represented by the dotted line). Drop deformation is then evaluated by computing the deformation parameter $D = (L - B)/(L + B)$, with L and B the major and minor axes, respectively.

(vi) Finally, the Cahn–Hilliard equation is solved on the FG to obtain the new value of the phase-field, $\hat{\phi}^{n+1}$.

A flowchart with the steps required to advance in time the solution, from step n to $n + 1$, is sketched in Fig. 2. Hat notation is used to identify the spectral representation of the variables.

4 Validation

The proposed method is benchmarked considering the case of a single drop immersed in a 2D laminar shear flow, as sketched in Fig. 3. A circular drop of diameter $d = 0.8h$ is placed at the center of a plane channel, in which the top and bottom walls move at a constant velocity, u_w, but in opposite directions. The main parameters that control drop deformation are the capillary number and the viscosity ratio between the two phases. The capillary number controls the relative importance of viscous and surface tension forces and can be computed as follows:

$$\text{Ca} = \frac{\text{We}}{\text{Re}} \frac{d}{2h} \qquad (26)$$

where the ratio $d/2h$ is used to rescale the capillary number on the drop diameter (instead of the channel half-height). We consider three values of the Capillary number: $\text{Ca} = 0.0625$, $\text{Ca} = 0.1250$, and $\text{Ca} = 0.1875$, and two values of the viscosity ratio $\eta_r = 0.1$ (drop less viscous than the continuous phase) and $\eta_r = 1$ (same viscosity for both phases). The Reynolds number—evaluated for this benchmark using the wall velocity—is kept constant among all simulations, $\text{Re} = 0.1$.

The initial condition for the flow field is a linear velocity profile for the streamwise velocity, u_x, along the wall-normal direction, z, while the wall-normal velocity is set to zero. The phase-field, ϕ, is initialized so that the drop is located at the center of the channel. The computational domain has dimensions $L_x \times L_z = 2\pi h \times 2h$ along the x and z directions, respectively.

For each combination of the capillary number and viscosity ratio, we kept fixed the grid resolution used for the NS equations ($N_x \times N_z = 256 \times 257$) and we employed three different grid resolutions for the CH equation: (i) a base grid (labeled $G1$), consisting of $N_x \times N_z = 256 \times 257$ grid points along the streamwise (x) and the wall-normal (z) direction, respectively (i.e., same grid used for NS); (ii) a second grid, two times finer than the base grid (case $G2$), consisting of $N_x \times N_z = 512 \times 513$ grid points along x and z directions; and (iii) a third grid, three times finer than the base grid (labeled $G3$), consisting of $N_x \times N_z = 768 \times 769$ grid points along the x and z directions. Note that, as the grid resolution employed for the CH equation is increased, the value of the Cahn number, Ch, is also decreased, so to have always a minimum of three

grid points across the thin interfacial layer [69]. Accordingly, the Péclet number is set using the scaling $\text{Pe} = 1/\text{Ch}$. As the thin interfacial layer is represented by at least three grid points, using larger refinement factors may not be beneficial from an accuracy point of view. Indeed, this can reduce the accuracy of the representation of the surface tension forces and of density/viscosity variations, which are computed on the BG. An overview of the simulation parameters is given in Table 1.

To compare present results with previous literature studies [74–76], we evaluate the drop deformation by computing the deformation parameter, D. Indicating with L and B are the major and minor axes of the deformed drop (see the sketch in Fig. 3), the deformation parameter can be computed as follows:

$$D = \frac{L - B}{L + B} \qquad (27)$$

An analytical solution for the behavior of D as a function of the capillary number was obtained by Taylor [74,75] for an unbounded flow, and later extended by Shapira and Haber [76] to account for lateral confinement effects

$$D = \frac{16 + 19\eta_r}{16 + 16\eta_r} \text{Ca} \left[1 + C_{\text{SH}} \frac{3.5}{2} \left(\frac{d}{4h} \right)^3 \right] \qquad (28)$$

where $C_{\text{SH}} = 5.6996$ is a numerical coefficient [76]. This equation is proven to be accurate also for 2D and 3D drops at small Ca, i.e., in the limit of small deformations [77–79].

Table 1 Summary of the parameters used to study the drop deformation in a shear flow

Code	Refinement factor, M_i	Grid NS	Grid CH	Ch	Pe
$G1$	1×1	256×257	256×257	0.0200	50
$G2$	2×2	256×257	512×513	0.0100	100
$G3$	3×3	256×257	768×769	0.0067	150

Three values of the Capillary number, $\text{Ca} = 0.0625$, $\text{Ca} = 0.1250$, and $\text{Ca} = 0.1875$, and two values of the viscosity ratio $\eta_r = 0.1$ and $\eta_r = 1$, have been considered. For each combination of the capillary number and viscosity ratio, three simulations with different refinement factors have been performed. Specifically, the grid resolution of the NS equations is kept fixed ($N_x \times N_z = 256 \times 257$, grid NS), while the grid resolution of the CH equations (grid CH) is refined by the refinement factors, M_i. The simulations are labeled according to the refinement factor used: $G1$ indicates a refinement factor $M_i = 1$ (i.e., the same grid); $G2$ indicates a refinement factor $M_i = 2$, and $G3$ a refinement factor $M_i = 3$ (along all directions).

The behavior of the deformation parameter, D, as a function of the capillary number, Ca, is shown in Fig. 4: Panel a refers to the cases with drop-to-fluid viscosity ratio $\eta_r = 0.1$, while panel b refers to the cases with drop-to-fluid viscosity ratio $\eta_r = 1$. For all considered cases, we find a good agreement between the numerical simulations (symbols, each referring to a specific grid resolution for the phase-field variable), and the analytical solution, with minor differences for the viscosity ratio $\eta_r = 0.1$ (discrepancy between theoretical and numerical results below 5%). In addition, we observe almost no difference between the results obtained by the grid $G1$ (same grid for NS and CH), grid $G2$ (CH grid two times finer than the NS grid), and grid $G3$ (CH grid three times finer than the NS grid). This shows the consistency of the proposed implementation and suggests that, when the flow-field is resolved on a fine enough grid, the dual-grid approach gives a final result that is comparable to the result that could be obtained by a simulation performed on the finer grid for both velocity and phase-field variables.

In the idea of performing large-scale simulations, it is important to evaluate the computational efficiency of the proposed technique. To evaluate it, we measure the wall-clock time required for a single time-step (Fig. 5(a)) and the memory usage (Fig. 5(b)) using different refinement factors, M_i. The results are reported normalized considering as reference the same case run using the finer grid for both the Navier–Stokes and Cahn–Hilliard equations. For example, in case of a refinement factor equal to $M_i = 3$, the results are normalized considering a simulation performed on a grid equal to $M_x N_x \times M_z N_z = 768 \times 769$ (i.e., the finer grid resolution) for both NS and CH equations. Current results indicate that, using the dual-grid approach, it is possible to save up to 27% in wall-clock time and memory usage for a refinement factor equal to 2 (i.e., CH is solved on
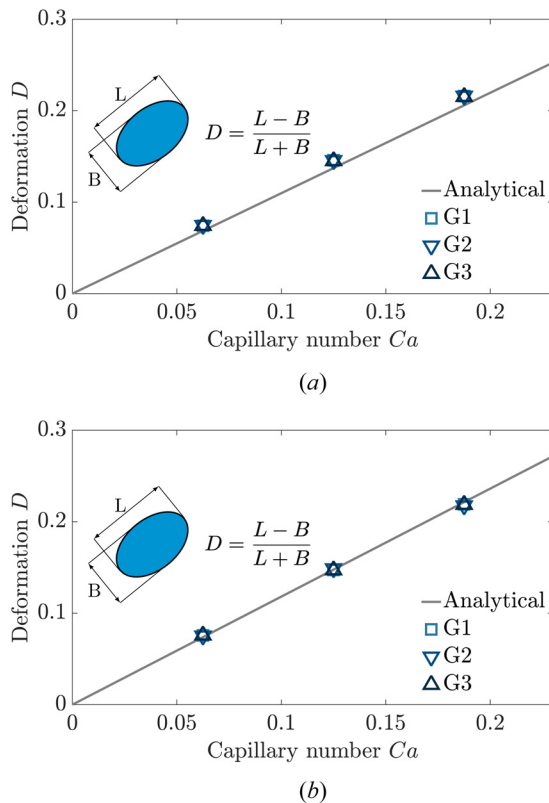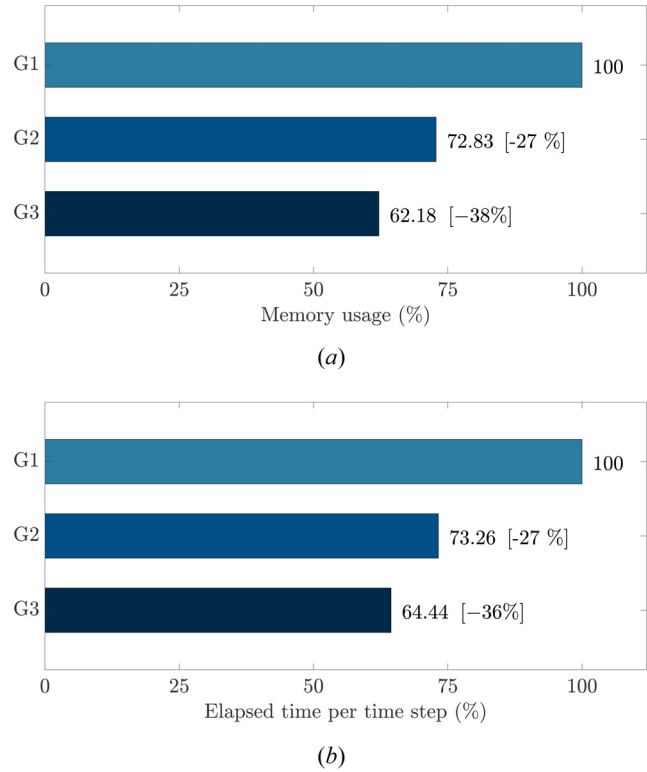

(a)

(b)

Fig. 5 Computational efficiency (lower is better) of the dual grid approach: elapsed time (wall-clock) for a time-step (panel *a*) and memory usage (panel *b*). Results are normalized by the corresponding values obtained when the finer grid is used for both the Navier–Stokes and Cahn–Hilliard equations. (■) refer to case *G*1 (same grid), (■) to case *G*2 (refinement factor equal to 2), and (■) to case *G*3 (refinement factor equal to 3). The same high-performance computing-cluster and setup were used, and the simulations were performed using the same number of MPI tasks (32).

a grid that is two times finer than that used for NS, case $G2$), and up to 38% in time and memory for a refinement factor of 3 (i.e., CH is solved on a grid that is three times finer than that used for NS, case $G3$), compared to the case in which the finest grid is used for both CH and NS. The efficiency of the dual-grid approach increases in 3D cases (not shown here). Specifically, we observe a reduction of the elapsed time per time-step up to 57% and a reduction of the memory usage up to 46% for an expansion factor equal to 3 (equal along all directions).

5 Breakage of a Liquid Sheet by Turbulence

The applicability of the proposed method to more computationally intensive and scientifically relevant cases is considered here, by studying the breakage of a liquid sheet in turbulence [4,80,81]. With reference to Fig. 6, a thin liquid sheet, thickness $0.15h$, is initially located at the center of a turbulent channel in which the flow is driven by an imposed pressure gradient. At the two walls, no-slip conditions are enforced for the velocity field, while no-flux conditions are enforced for the phase-field variable and its second derivative. Periodicity is implicitly applied along x and y for all variables. The initial condition for the flow-field is taken from a preliminary direct numerical simulations of a single-phase fully developed turbulent channel flow at $\text{Re}_\tau = 150$, complemented by a proper definition of the initial distribution of the phase, ϕ, so that a thin liquid sheet (thickness $0.15h$) is placed at the channel centerline. The liquid sheet and the carrier fluid have the same density and viscosity ($\rho_r = \eta_r = 1$), while the Weber number has been set to $\text{We} = 3$.

We perform three different simulations (see Table 2) considering a computational domain having dimensions $L_x \times L_y \times L_z =$

(a)

(b)

Fig. 4 Behavior of the deformation parameter, *D*, (see sketch in Fig. 3) as a function of the capillary number, Ca, for a drop in a 2D shear flow. The numerical results (symbols) are compared against the analytical predictions [76]. Two different viscosity ratios are considered: η_r=0.1 (panel *a*) and η_r=1.0 (panel *b*). The different symbols refer to the different refinement factors employed: squares, case *G*1; down-facing triangles, case *G*2; upward-facing triangles, case *G*3.
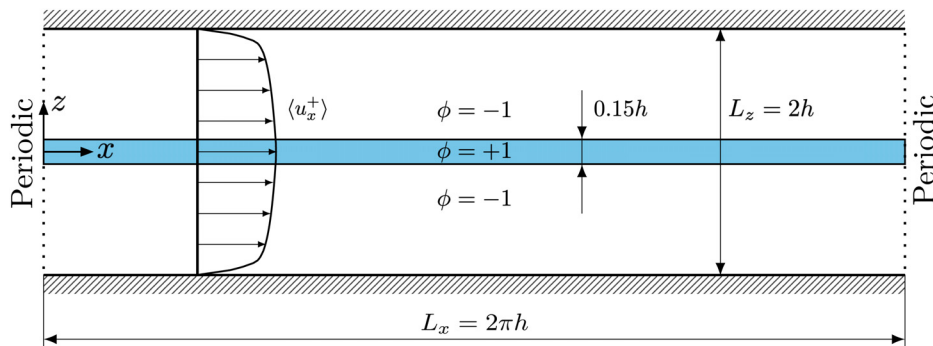
Fig. 6 Sketch of the simulation setup used to investigate the breakage of a liquid sheet in a turbulent channel flow at a friction Reynolds number Re$_\tau$=150. A thin liquid sheet, thickness 0.15h, is initially placed at the center of a plane channel. The channel has dimensions $L_x \times L_y \times L_z$=2$\pi h \times \pi h \times 2h$. A sketch of the mean streamwise velocity profile, $\langle u_x^+ \rangle$, is also shown.

Table 2 Summary of the parameters used to study the breakage of a liquid sheet in a turbulent channel flow at a Reynolds number of Re$_\tau$=150

Code	Refinement, M_i	Grid NS	Grid CH	Ch	Pe
$G1$	$1 \times 1 \times 1$	$256 \times 128 \times 513$	$256 \times 128 \times 513$	0.0200	50
$G2$	$2 \times 2 \times 2$	$256 \times 128 \times 513$	$512 \times 256 \times 1025$	0.0100	100
$G3$	$3 \times 3 \times 3$	$256 \times 128 \times 513$	$768 \times 384 \times 1537$	0.0067	150

We keep the grid resolution used to solve for the NS equations fixed, and we increase (introducing a refinement factor, M_i) the grid resolution used to solve for the CH equation. Simulations are labeled based on the employed refinement factor: case $G1$ (unitary refinement factor, same grid for NS and CH); case $G2$ (refinement factor $M_i = 2$ along each direction); case $G3$ (refinement factor $M_i = 3$ along each direction). As the grid resolution used for the CH equation is increased, the Cahn number, Ch, is decreased.

$2\pi h \times \pi h \times 2h$ along the streamwise (x), spanwise (y), and wall-normal directions (z), respectively. Assessment of the domain size (not shown here for brevity) has been performed upon comparison of the flow statistics against available datasets. For all three simulations, the flow-field is solved using a computational grid consisting of $N_x \times N_y \times N_z = 256 \times 128 \times 513$ points, which grants resolution of the flow-field down to the Kolmogorov scale. Specifically, the resulting grid spacing in wall units is: $\Delta x^+ = \Delta y^+ = 3.69$ w.u. and $\Delta z_{max}^+ = 0.92$ w.u. (at the channel center). The Cahn–Hilliard equation is discretized on progressively refined grids. In particular, we employ $N_x \times N_y \times N_z = 256 \times 128 \times 513$ for $G1$ (refinement factor $M_i = 1$ along each direction), $N_x \times N_y \times N_z = 512 \times 256 \times 1025$ for $G2$ (refinement factor $M_i = 2$ along each direction), and $N_x \times N_y \times N_z = 768 \times 384 \times 1537$ for $G3$ (refinement factor $M_i = 3$ along each direction). This gives a Cahn number (and a corresponding Péclet number, Pe $= 1/$Ch) Ch $= 0.02$ (Pe $= 50$) for $G1$, Ch $= 0.01$ (Pe $= 100$) for $G2$, and Ch $= 0.0067$ (Pe $= 150$) for $G3$, so to guarantee that the interfacial transition layer is represented by at least three grid points. We recall that the computational grid is uniform along x and y, whereas it is stretched along the wall-normal direction where Chebyshev polynomials are employed. This leads to a grid resolution that is finer near the two walls and coarser at the channel center. An overview of the simulation parameters is given in Table 2.

5.1 Results. The turbulent flow exerts shear and normal forces on the thin liquid sheet, and leads to its fragmentation in drops of different sizes. To characterize this transient dynamics, we consider the behavior of the normalized interfacial area, $A(t^+)/A_0$, (defined as the area separating the two liquid phases, with A_0 its initial value). The results are shown in Fig. 7, for the three different cases
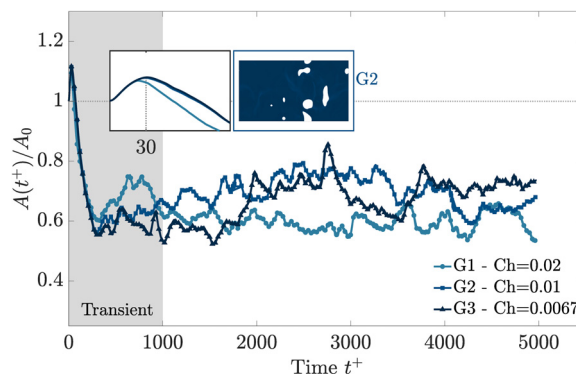

Fig. 7 Evolution of the total interfacial area, $A(t^+)$, normalized by the initial area, A_0. Results from the three simulations $G1$, $G2$, and $G3$ are shown using different symbols and colors, from light to dark. The gray area represents the initial transient, after which a statistically steady condition is reached. The insets focus on the initial transient behavior of $A(t^+)/A_0$ (for $0 < t^+ < 100$, left inset) and on the deformation of the thin sheet (seen from the top) at $t^+ \simeq 100$ for simulation $G2$ (right inset).

considered here. All three simulations follow a qualitatively similar behavior. Starting from the flat and straight initial condition, the thin liquid sheet is first stretched and deformed by the flow. This induces the initial increase of the interfacial area, $A(t^+)$, with a maximum at about $t^+ \simeq 30$ (see inset). After this point, the thin liquid sheet is so stretched and narrow, that it breaks down forming ligaments and drops (primary breakup). This induces a sharp decrease in the interface area, $A(t^+)$. Later in time, when the drops break up into smaller drops, the overall interfacial area slightly increases again (at about $t^+ \simeq 400$). This finally leads to a statistically steady-state ($t^+ > 1000$, white area), during which breakage and coalescence of drops occur simultaneously, and dynamically balance each other, so to induce fluctuations of interfacial area around a constant value.

We can observe that the grid resolution employed for the solution of the Cahn–Hilliard equation, and thus the value of the Cahn number, Ch, that can be adopted, has an influence on the dynamics. In particular, from a vis-a-vis comparison between the results obtained for $G1$, $G2$, and $G3$, we notice that the smaller is Ch, the larger the increase of area during the initial transient, and also the larger the increase of the steady-state area. Indeed, thanks to the higher resolution (and the resulting smaller Cahn number) that can be employed, higher deformations and finer/smaller drops and structures can be described as the grid resolution is increased. Interestingly, while the difference between the case $G1$ and $G2$ is clearly visible, the difference between the cases $G2$ and $G3$ is less pronounced and the two curves reach similar steady-state values.
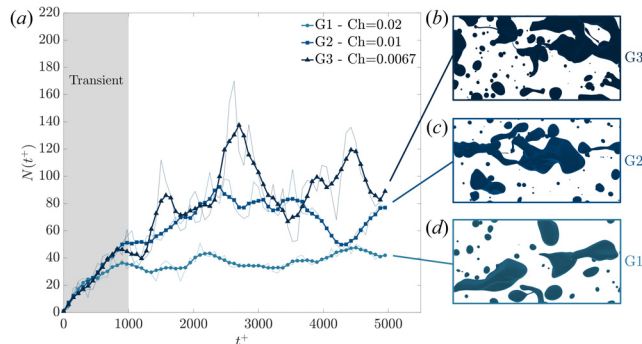
Fig. 8 Time behavior of the number of drops, $N(t^+)$, for the three simulations, $G1$, $G2$, and $G3$. The shaded area roughly represents the extension of the initial transient, after which a pseudo-steady-state condition is reached ($t^+ > 1000$). Qualitative pictures (panels *b–d*), show a snapshot of the drops at the end of the simulation ($t^+ \simeq 5000$). Thick lines represent the data filtered using a running average procedure while thin lines are used to identify the raw signal.

Finally, it is also worth mentioning that for the case $G3$ (Ch $=$ 0.0067), the thickness of the thin interfacial layer, which in wall units can be computed as 4.1ChRe$_\tau \simeq 4$ w.u., is comparable to the Kolmogorov length-scale evaluated at the channel center, where most of the drops gather ($\eta_k^+ = 3.45$ w.u. for the Reynolds number here considered). This indicates that Kolmogorov-size drops can be accurately described using the finer grid resolution (case $G3$).

The behavior of the interfacial area described above reflects a corresponding evolution of the number of drops. Figure 8 shows the temporal evolution of the number of drops, $N(t^+)$, for the different grid resolutions employed ($G1$, $G2$, and $G3$). In general, we can observe an increase in the number of drops by increasing the grid resolution and thus decreasing the Cahn number. This is due to the fact that a finer grid allows for the description of smaller drops with respect to a coarser grid. Considering the different cases, we notice that the larger difference can be observed between the cases $G1$ and $G2$ while a smaller difference is observed between the cases $G2$ and $G3$. The main difference between the cases $G2$ and $G3$ is in the fluctuations of the number of drops: the case $G3$ is characterized by much larger fluctuations. These fluctuations can be linked to the drop dynamics, which is characterized by the simultaneous occurrence of breakage and coalescence events, and by the interactions of drops with a turbulent flow (which is characterized by velocity/pressure fluctuations). Indeed, the number of drops is the result of the competition between breakage events (which increase the number of drops) and coalescence events (which reduce the number of drops). The number of drops in the channel can be described by the following population balance equation [19,82–84]:

$$\frac{dN(t^+)}{dt^+} = \dot{N}_b(t^+) - \dot{N}_c(t^+) \tag{29}$$

where $\dot{N}_b(t^+)$ and $\dot{N}_c(t^+)$ are the drops breakage and coalescence rates, which can be estimated by counting the number of breakup and coalescence events over a given time interval, Δt^+. From the above equation, we can appreciate how fluctuations in these rates can induce fluctuations also in the number of drops. In addition, it must be also pointed out that the number of breakage and coalescence rates depends also on the number of drops, $N(t^+)$, present at a certain time instant, in such a way that larger $dN(t^*)/dt^+$ are expected for larger $N(t^+)$ [19,43]. In this context, a smaller value of Ch, which gives the possibility of capturing the dynamics of thin ligaments and smaller drops, can give larger values of $N(t)$. Note indeed the rich dynamics (thin liquid bridges and ligaments, small drops) that can be progressively captured by reducing the value of Ch (see inset in Fig. 8, from $G1$ to $G3$). These small interfacial structures have been also recently observed in numerical investigations of drop breakage

in homogenous isotropic turbulence using the volume-of-fluid method [85–87].

A quantity of fundamental importance in the study of mass/momentum and heat exchanges in a drop-laden turbulent flow is the drop size distribution (DSD). The DSD is the probability density function of the drop diameter, and therefore provides a measure of the number of drops as a function of their characteristic size. Since in the present case drops can undergo large deformations, we consider the equivalent diameter as characteristic size [69]

$$d_{eq}^+ = \left(\frac{6V_i^+}{\pi}\right)^{\frac{1}{3}} \tag{30}$$

where V_i^+ is the dimensionless volume of the ith drop expressed in wall-units. Compared with the overall number of drops presented above, the DSD provides a more insightful picture of the topology of the dispersed phase, as it evaluates more precisely the number of drops for each characteristic size. For instance, for a fixed volume fraction, a large number of small drops identify a larger surface-to-volume ratio, hence maximizing the transport processes across their surface. A wide range of different drop diameters is expected as a consequence of coalescence (drop–drop interaction) and breakage (drop–turbulence interaction) events.

The breakage of a drop is the outcome of the competition between destabilizing actions like shear forces and turbulent fluctuations—which tend to deform the drop—and stabilizing surface tension forces—which tend to preserve the drop shape. When destabilizing forces are larger than surface tension forces, a drop breaks. In contrast, a coalescence event is observed when two drops come close to each other, so that the small liquid film that separates the drops drains and leads to the formation of a coalescence bridge.

From a balance between stabilizing actions (surface tension forces) and destabilizing actions (shear forces and turbulent fluctuations), the maximum size of a drop that can be transported by turbulence without breaking, the Kolmogorov-Hinze diameter can be computed [88,89]. For a turbulent channel flow configuration, the Kolmogorov-Hinze scale can be computed as follows [19,45,64,90]:

$$d_H^+ = 0.725\left(\frac{We}{Re_\tau}\right)^{-3/5}|\epsilon_c^+|^{-2/5} \tag{31}$$

where ϵ_c^+ is the turbulent dissipation at the center of the channel, where deformable drops migrate. The Kolmogorov-Hinze scale is not an exact threshold and should be taken more as a reference scale about which the dynamics of drops change behavior (from surface tension to the inertia-dominated regime) [91]. Results of the DSD obtained by present simulations are shown in Fig. 9. In particular, we compare the DSD curves—which are computed after the steady-state condition is attained ($t^+ > 1000$)—for the three different grid resolutions employed in this study. The value of the reference Kolmogorov-Hinze diameter, d_H^+, is explicitly indicated by the vertical dashed line. Also shown in Fig. 9 are the theoretical behaviors proposed in the literature [14,92–94]. In particular, Garrett et al. [92] proposed a power-law scaling for drops smaller than the Kolmogorov-Hinze scale (coalescence-dominated regime)

$$P(d^+) \propto d^{+-3/2} \tag{32}$$

and a power-law scaling with a different exponent for drops larger than the Kolmogorov-Hinze scale (breakage-dominated regime)

$$P(d^+) \propto d^{+-10/3} \tag{33}$$

Results are shown in Fig. 9. We note that regardless of the grid resolution, all DSDs present a similar behavior, characterized by a transition between the two theoretical scalings occurring around the Kolmogorov-Hinze diameter, d_H^+. The main effect of using a finer grid (in particular $G3$) is the presence of a larger number of smaller
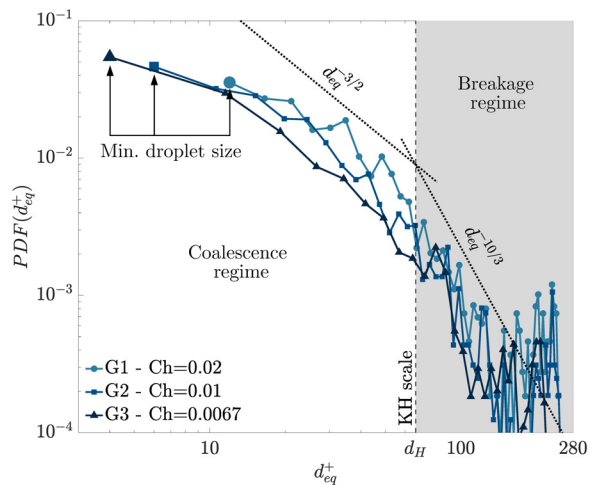
Fig. 9 DSD in log–log scale, for the three simulations $G1$ (circles), $G2$ (squares), and $G3$ (triangles). The theoretical scalings, $d_{\mathrm{eq}}^{+\,-3/2}$ and $d_{\mathrm{eq}}^{+\,-10/3}$, for the coalesce-dominated and the breakage-dominated regimes are also represented by a dotted line. The Kolmogorov-Hinze scale, d_H^+, is indicated with a vertical dashed line.

drops (with diameter of about $\simeq 6$ wall units), given the better representation obtained for these drops. We recall here that this can be also qualitatively assessed in Fig. 8, by looking at the distribution of drops at the channel center for the different cases ($G1$, $G2$, and $G3$), at the time instant ($t^+ \simeq 5000$). The capability of finer grids to capture small scales dynamics is clearly visible (see, for example, the formation of thin liquid bridges/ligaments for simulation $G3$, Fig. 8(*b*)). Interesting indications about the influence of the grid resolution (i.e., value of Ch) on the effectiveness of the simulation in capturing the drops dynamics can be inferred by looking at the cumulative distribution function, which can be expressed as the integral of the DSD curves shown in Fig. 9

$$\mathrm{CDF}(d_{\mathrm{eq}}^+) = \int_0^{d_{\mathrm{eq}}^+} \mathrm{PDF}(\tau)\, d\tau \qquad (34)$$

where τ is a dummy variable sweeping the considered range of diameters. The $\mathrm{CDF}(d_{\mathrm{eq}}^+)$ represents the fraction of the overall
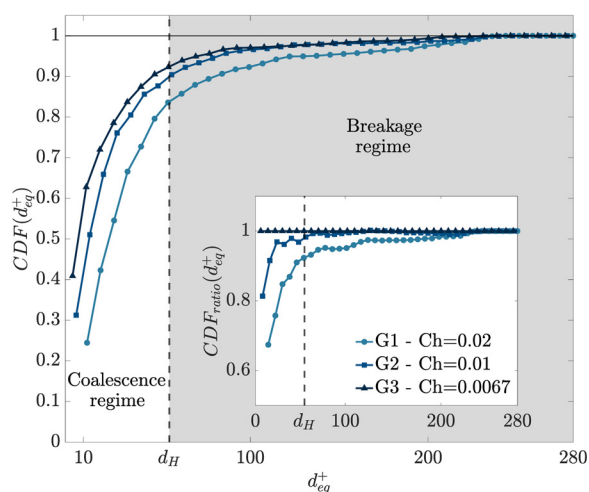

Fig. 10 CDF of the equivalent drop diameter, measured based on the DSD distribution of Fig. 9. The ratio between the CDF measured for the different simulations, i.e., CDF($G1$)/CDF($G3$), CDF($G2$)/CDF($G3$), and CDF($G3$)/CDF($G3$), i.e., an horizontal line at value 1—is shown in the inset.

volume of drops having diameter smaller than d_{eq}^+. Results for the three simulations $G1$, $G2$, and $G3$ are shown in Fig. 10. We notice that, regardless of the value of Ch, the cumulative distribution function (CDF) increases monotonically for increasing d_{eq}^+, and reaches the value CDF $= 1$ when even the largest drop in the domain ($d_{\mathrm{eq}}^+ \simeq 200$) has been considered in the calculation. As expected, the smaller is Ch, the better is the representation of small drops, and therefore the higher is the local value of the CDF in the region of small d_{eq}^+. In other terms, the number of small drops is higher at smaller Ch. What is also very interesting to note is the tendency for simulation $G2$ (Ch $= 0.01$) to collapse on top of simulation $G3$ (Ch $= 0.0067$) for $d_{\mathrm{eq}}^+ \geq d_H^+$. This indicates that simulation $G2$ captures very well the distribution (and in turn the dynamics) of drops with $d_{\mathrm{eq}}^+ \geq d_H^+$. This tendency is explicitly shown in the inset of Fig. 9, where we plot the ratio between the CDF of simulations $G1$ and $G2$ compared to that of simulation $G3$, i.e., CDF($G1$)/CDF($G3$) and CDF($G2$)/CDF($G3$). It is apparent that CDF($G2$)/CDF($G3$) $\rightarrow 1$ for $d_{\mathrm{eq}}^+ \geq d_H^+$. This observation, along with all other considerations given before (on the overall interface area, number of drops and DSD, see Figs. 7–9) suggests that the use of Ch $= 0.01$ in the simulation of drop-laden turbulence represents a good compromise between accuracy (i.e., capability of capturing the overall dynamics of drops) and computational efficiency. Naturally, when the research interest is on the description of ligaments and liquid bridges formation and breakup, then the use of a smaller Ch is recommended.

6 Conclusions

In this work, we have presented a dual-grid approach for direct numerical simulations of turbulent multiphase flows, and using the PFM to track the interface shape, deformation, and topological changes. The approach is based on a pseudo-spectral discretization of the governing equations (continuity, Navier–Stokes, and Cahn–Hilliard). The dual-grid approach is based on the definition of two different computational grids: a base grid for the solution of the Navier–Stokes equations, and a finer grid for the solution of the Cahn–Hilliard equation (phase-field method). It is important to note that the computational grid used for the solution of the Navier–Stokes equations must be fine enough to solve the flow-field down to the smallest flow scale (order of the Kolmogorov length scale).

The computational efficiency of the proposed approach have been evaluated in terms of elapsed time per time-step and memory usage for the case of a drop that deforms in a two-dimensional shear flow, showing a reduction up to $\simeq 40\%$ in term of computational time and memory usage for 2D simulations and up to 50% for 3D simulations (compared to the case in which all equations are solved on the same, finer, grid). The applicability of the approach to a realistic three-dimensional case has also been discussed, upon evaluation of the breakage of a thin liquid sheet inside a turbulent channel flow. Results show that, by increasing the grid resolution used to describe the phase-field (and consequently decreasing the Cahn number), the dynamics of liquid bridges/ligaments breakup, and the formation of small drops can be progressively better captured. In addition, our results seem to suggest that a resolution for the phase-field corresponding to Ch $= 0.01$ represents a good compromise between the multiphase flow description and the computational cost, in particular for the simulation of drop-laden turbulence (this threshold can be slightly relaxed when the interface does not undergo frequent breakups).

Data Availability Statement

The datasets generated and supporting the findings of this article are obtainable from the corresponding author upon reasonable request.

References

[1] Melville, W. K., 1996, "The Role of Surface-Wave Breaking in Air-Sea Interaction," Annu. Rev. Fluid Mech., **28**, p. 279.

[2] Villermaux, E., and Bossa, B., 2009, "Single-Drop Fragmentation Determines Size Distribution of Raindrops," Nat. Phys., **5**, p. 697.

[3] Deike, L., 2022, "Mass Transfer at the Ocean–Atmosphere Interface: The Role of Wave Breaking, Droplets, and Bubbles," Annu. Rev. Fluid Mech., **54**, pp. 191–224.

[4] Ling, Y., Fuster, D., Tryggvason, G., and Zaleski, S., 2019, "A Two-Phase Mixing Layer Between Parallel Gas and Liquid Streams: Multiphase Turbulence Statistics and Influence of Interfacial Instability," J. Fluid Mech., **859**, p. 268.

[5] Karathanassis, I. K., Koukouvinis, F. P., and Gavaises, M., 2019, "Multiphase Phenomena in Diesel Fuel Injection Systems," *Simulations and Optical Diagnostics for Internal Combustion Engines (Energy, Environment, and Sustainability)*, Springer, Singapore.

[6] Gorokhovski, M., and Herrmann, M., 2008, "Modeling Primary Atomization," Annu. Rev. Fluid Mech., **40**, p. 343.

[7] Bourouiba, L., Dehandschoewercker, E., and Bush, J. W., 2014, "Violent Expiratory Events: On Coughing and Sneezing," J. Fluid Mech., **745**, pp. 537–563.

[8] Balachandar, S., Zaleski, S., Soldati, A., Ahmadi, G., and Bourouiba, L., 2020, "Host-to-Host Airborne Transmission as a Multiphase Flow Problem for Science-Based Social Distance Guidelines," Int. J. Multiphase Flow, **132**, p. 103439.

[9] Wang, J., Alipour, M., Soligo, G., Roccon, A., De Paoli, M., Picano, F., and Soldati, A., 2021, "Short-Range Exposure to Airborne Virus Transmission and Current Guidelines," Proc. Natl. Acad. Sci. U. S. A., **118**, p. e2105279118.

[10] Magar, V., and Pedley, T. J., 2005, "Average Nutrient Uptake by a Self-Propelled Unsteady Squirmer," J. Fluid Mech., **539**, pp. 93–112.

[11] Metselaar, L., Yeomans, J. M., and Doostmohammadi, A., 2019, "Topology and Morphology of Self-Deforming Active Shells," Phys. Rev. Lett., **123**(20), p. 208001.

[12] Tryggvason, G., Thomas, S., Lu, J., and Aboulhasanzadeh, B., 2010, "Multiscale Issues in DNS of Multiphase Flows," Acta Math. Sci., **30**(2), pp. 551–562.

[13] Thomas, S., Esmaeeli, A., and Tryggvason, G., 2010, "Multiscale Computations of Thin Films in Multiphase Flows," Int. J. Multiphase Flow, **36**, pp. 71–77.

[14] Soligo, G., Roccon, A., and Soldati, A., 2021, "Turbulent Flows With Drops and Bubbles: What Numerical Simulations Can Tell Us—Freeman Scholar Lecture," ASME J. Fluids Eng., **143**(8), p. 080801.

[15] Hirt, C., and Nicholos, B., 1981, "Volume of Fluid (VOF) Method for the Dynamics of Free Boundaries," J. Comput. Phys., **39**(1), pp. 201–225.

[16] Osher, S., and Sethian, J., 1994, "A Level Set Approach for Computing Solutions to Incompressible Two-Phase Flow," J. Comput. Phys., **114**(1), pp. 146–159.

[17] Jacqmin, D., 1999, "Calculation of Two-Phase Navier–Stokes Flows Using Phase-Field Modeling," J. Comput. Phys., **155**(1), pp. 96–127.

[18] Dodd, M. S., and Ferrante, A., 2016, "On the Interaction of Taylor Length Scale Size Droplets and Isotropic Turbulence," J. Fluid Mech., **806**, pp. 356–412.

[19] Soligo, G., Roccon, A., and Soldati, A., 2019, "Breakage, Coalescence and Size Distribution of Surfactant-Laden Droplets in Turbulent Flow," J. Fluid Mech., **881**, p. 244.

[20] Berger, M. J., and Oliger, J., 1984, "Adaptive Mesh Refinement for Hyperbolic Partial Differential Equations," J. Comput. Phys., **53**(3), pp. 484–512.

[21] Berger, M. J., and Colella, P., 1989, "Local Adaptive Mesh Refinement for Shock Hydrodynamics," J. Comput. Phys., **82**(1), pp. 64–84.

[22] Popinet, S., 2003, "Gerris: A Tree-Based Adaptive Solver for the Incompressible Euler Equations in Complex Geometries," J. Comput. Phys., **190**(2), pp. 572–600.

[23] Greaves, D., 2004, "A Quadtree Adaptive Method for Simulating Fluid Flows With Moving Interfaces," J. Comput. Phys., **194**(1), pp. 35–56.

[24] Fuster, D., Bagué, A., Boeck, T., Le Moyne, L., Leboissetier, A., Popinet, S., Ray, P., Scardovelli, R., and Zaleski, S., 2009, "Simulation of Primary Atomization With an Octree Adaptive Mesh Refinement and VOF Method," Int. J. Multiphase Flow, **35**(6), pp. 550–565.

[25] Laurmaa, V., Picasso, M., and Steiner, G., 2016, "An Octree-Based Adaptive Semi-Lagrangian VOF Approach for Simulating the Displacement of Free Surfaces," Comput. Fluids, **131**, pp. 190–204.

[26] Sussman, M., Almgren, A. S., Bell, J. B., Colella, P., Howell, L. H., and Welcome, M. L., 1999, "An Adaptive Level Set Approach for Incompressible Two-Phase Flows," J. Comput. Phys., **148**(1), pp. 81–124.

[27] Strain, J., 1999, "Tree Methods for Moving Interfaces," J. Comput. Phys., **151**(2), pp. 616–648.

[28] Losasso, F., Gibou, F., and Fedkiw, R., 2004, "Simulating Water and Smoke With an Octree Data Structure," ACM Trans. Graphics, **23**(3), pp. 457–462.

[29] Losasso, F., Fedkiw, R., and Osher, S., 2006, "Spatially Adaptive Techniques for Level Set Methods and Incompressible Flow," Comput. Fluids, **35**(10), pp. 995–1010.

[30] Herrmann, M., 2008, "A Balanced Force Refined Level Set Grid Method for Two-Phase Flows on Unstructured Flow Solver Grids," J. Comput. Phys., **227**(4), pp. 2674–2706.

[31] Mirzadeh, M., Guittet, A., Burstedde, C., and Gibou, F., 2016, "Parallel Level-Set Methods on Adaptive Tree-Based Grids," J. Comput. Phys., **322**, pp. 345–364.

[32] Gibou, F., Fedkiw, R., and Osher, S., 2018, "A Review of Level-Set Methods and Some Recent Applications," J. Comput. Phys., **353**, pp. 82–109.

[33] Fakhari, A., Bolster, D., and Luo, L.-S., 2017, "A Weighted Multiple-Relaxation-Time Lattice Boltzmann Method for Multiphase Flows and Its Application to Partial Coalescence Cascades," J. Comput. Phys., **341**, pp. 22–43.

[34] Watanabe, S., and Aoki, T., 2021, "Large-Scale Flow Simulations Using Lattice Boltzmann Method With AMR Following Free-Surface on Multiple GPUs," Comput. Phys. Commun., **264**, p. 107871.

[35] Ceniceros, H. D., Nos, R. L., and Roma, A. M., 2010, "Three-Dimensional, Fully Adaptive Simulations of Phase-Field Fluid Models," J. Comput. Phys., **229**(17), pp. 6135–6155.

[36] Khanwale, M. A., Lofquist, A. D., Sundar, H., Rossmanith, J. A., and Ganapathysubramanian, B., 2020, "Simulating Two-Phase Flows With Thermodynamically Consistent Energy Stable Cahn-Hilliard Navier-Stokes Equations on Parallel Adaptive Octree Based Meshes," J. Comput. Phys., **419**, p. 109674.

[37] Ostilla-Monico, R., Yang, Y., van der Poel, E., Lohse, D., and Verzicco, R., 2015, "A Multiple-Resolution Strategy for Direct Numerical Simulation of Scalar Turbulence," J. Comput. Phys., **301**, p. 308.

[38] Ding, H., and Yuan, C.-J., 2014, "On the Diffuse Interface Method Using a Dual-Resolution Cartesian Grid," J. Comput. Phys., **273**, p. 243.

[39] Liu, H.-R., Ng, C. S., Chong, K. L., Lohse, D., and Verzicco, R., 2021, "An Efficient Phase-Field Method for Turbulent Multiphase Flows," J. Comput. Phys., **446**, p. 110659.

[40] Bazesefidpar, K., Brandt, L., and Tammisola, O., 2022, "A Dual Resolution Phase–Field Solver for Wetting of Viscoelastic Droplets," Int. J. Numer. Methods Fluids, **94**, p. 1517.

[41] Feng, W., Yu, P., Hu, S., Liu, Z.-K., Du, Q., and Chen, L.-Q., 2006, "Spectral Implementation of an Adaptive Moving Mesh Method for Phase-Field Equations," J. Comput. Phys., **220**(1), pp. 498–510.

[42] Burstedde, C., Wilcox, L. C., and Ghattas, O., 2011, "p4est: Scalable Algorithms for Parallel Adaptive Mesh Refinement on Forests of Octrees," SIAM J. Sci. Comput., **33**(3), pp. 1103–1133.

[43] Mangani, F., Soligo, G., Roccon, A., and Soldati, A., 2022, "Influence of Density and Viscosity on Deformation, Breakage, and Coalescence of Bubbles in Turbulence," Phys. Rev. Fluids, **7**, p. 053601.

[44] Mangani, F., Roccon, A., Zonta, F., and Soldati, A., 2024, "Heat Transfer in Drop-Laden Turbulence," J. Fluid Mech., **978**, p. A12.

[45] Giamagas, G., Zonta, F., Roccon, A., and Soldati, A., 2023, "Propagation of Capillary Waves in Two-Layer Oil–Water Turbulent Flow," J. Fluid Mech., **960**, p. A5.

[46] Anderson, D. M., McFadden, G. B., and Wheeler, A. A., 1998, "Diffuse-Interface Methods in Fluid Mechanics," Annu. Rev. Fluid Mech., **30**, p. 139.

[47] Roccon, A., Zonta, F., and Soldati, A., 2023, "Phase-Field Modeling of Complex Interface Dynamics in Drop-Laden Turbulence," Phys. Rev. Fluids, **8**, p. 090501.

[48] Badalassi, V., Ceniceros, H., and Banerjee, S., 2003, "Computation of Multiphase Systems With Phase Field Models," J. Comput. Phys., **190**, p. 371.

[49] Tóth, G. I., and Kvamme, B., 2015, "Analysis of Ginzburg-Landau-Type Models of Surfactant-Assisted Liquid Phase Separation," Phys. Rev. E, **91**, p. 032404.

[50] Scarbolo, L., Bianco, F., and Soldati, A., 2015, "Coalescence and Breakup of Large Droplets in Turbulent Channel Flow," Phys. Fluids, **27**(7), p. 073302.

[51] Yue, P., Zhou, C., and Feng, J., 2007, "Spontaneous Shrinkage of Drops and Mass Conservation in Phase-Field Simulations," J. Comput. Phys., **223**(1), pp. 1–9.

[52] Li, Y., Choi, J.-I., and Kim, J., 2016, "A Phase-Field Fluid Modeling and Computation With Interfacial Profile Correction Term," Commun. Nonlinear Sci. Numer. Simul., **30**, p. 84.

[53] Soligo, G., Roccon, A., and Soldati, A., 2019, "Mass-Conservation-Improved Phase Field Methods for Turbulent Multiphase Flow Simulation," Acta Mech., **230**, p. 683.

[54] Yue, P., Zhou, C., and Feng, J., 2010, "Sharp-Interface Limit of the Cahn–Hilliard Model for Moving Contact Lines," J. Fluid Mech., **645**, p. 279.

[55] Magaletti, F., Picano, F., Chinappi, M., Marino, L., and Casciola, C. M., 2013, "The Sharp-Interface Limit of the Cahn–Hilliard/Navier–Stokes Model for Binary Fluids," J. Fluid Mech., **714**, pp. 95–126.

[56] Prosperetti, A., and Tryggvason, G., 2009, *Computational Methods for Multiphase Flow*, Cambridge University Press, Cambridge, UK.

[57] Elghobashi, S., 2019, "Direct Numerical Simulation of Turbulent Flows Laden With Droplets or Bubbles," Annu. Rev. Fluid Mech., **51**(1), pp. 217–244.

[58] Lafaurie, B., Nardone, C., Scardovelli, R., Zaleski, S., and Zanetti, G., 1994, "Modelling Merging and Fragmentation in Multiphase Flows With SURFER," J. Comput. Phys., **113**(1), pp. 134–147.

[59] Gueyffier, D., Li, J., Nadim, A., Scardovelli, R., and Zaleski, S., 1999, "Volume-of-Fluid Interface Tracking With Smoothed Surface Stress Methods for Three-Dimensional Flows," J. Comput. Phys., **152**(2), pp. 423–456.

[60] Korteweg, D. J., 1901, "Sur la Forme Que Prennent Les Equations du Mouvements Des Fluides si L'on Tient Compte Des Forces Capillaires Causees Par Des Variations de Densite Considerables Mais Connues et Sur la Theorie de la Capillarite Dans L'hypothese D'une Variation Continue de la Densite," Arch. Neerl. Sci. Exactes Nat., **6**, pp. 1–24.

[61] Ding, H., Spelt, P. D., and Shu, C., 2007, "Diffuse Interface Model for Incompressible Two-Phase Flows With Large Density Ratios," J. Comput. Phys., **226**, p. 2078.

[62] Kim, J., 2012, "Phase-Field Models for Multi-Component Fluid Flows," Commun. Comput. Phys., **12**(3), pp. 613–661.

[63] Alpak, F. O., Riviere, B., and Frank, F., 2016, "A Phase-Field Method for the Direct Simulation of Two-Phase Flows in Pore-Scale Media Using a Non-Equilibrium Wetting Boundary Condition," Comput. Geosci., 20, p. 881.

[64] Roccon, A., De Paoli, M., Zonta, F., and Soldati, A., 2017, "Viscosity-Modulated Breakup and Coalescence of Large Drops in Bounded Turbulence," Phys. Rev. Fluids, 2, p. 083603.

[65] Kim, J., Moin, P., and Moser, R., 1987, "Turbulence Statistics in Fully Developed Channel Flow at Low Reynolds Number," J. Fluid Mech., 177, pp. 133–166.

[66] Speziale, C. G., 1987, "On the Advantages of the Vorticity-Velocity Formulation of the Equations of Fluid Dynamics," J. Comput. Phys., 73(2), pp. 476–480.

[67] Zonta, F., Marchioli, C., and Soldati, A., 2012, "Modulation of Turbulence in Forced Convection by Temperature-Dependent Viscosity," J. Fluid Mech., 697, pp. 150–174.

[68] Zonta, F., Onorato, M., and Soldati, A., 2012, "Turbulence and Internal Waves in Stably-Stratified Channel Flow With Temperature-Dependent Fluid Properties," J. Fluid Mech., 697, pp. 175–203.

[69] Soligo, G., Roccon, A., and Soldati, A., 2019, "Coalescence of Surfactant-Laden Drops by Phase Field Method," J. Comput. Phys., 376, p. 1292.

[70] Hussaini, M. Y., and Zang, T. A., 1987, "Spectral Methods in Fluid Dynamics," Annu. Rev. Fluid Mech., 19(1), pp. 339–367.

[71] Peyret, R., 2002, Spectral Methods for Incompressible Viscous Flow (Applied Mathematical Sciences, Vol. 148), Springer, New York.

[72] Turisini, M., Amati, G., and Cestari, M., 2024, "LEONARDO: A Pan-European Pre-Exascale Supercomputer for HPC and AI Applications," Jnl. Large-scale Res. Fac., 9(1).

[73] Yue, P., Feng, J. J., Liu, C., and Shen, J., 2004, "A Diffuse-Interface Method for Simulating Two-Phase Flows of Complex Fluids," J. Fluid Mech., 515, pp. 293–317.

[74] Taylor, G. I., 1932, "The Viscosity of a Fluid Containing Small Drops of Another Fluid," Proc. R. Soc. London, Ser. A, 138(834), pp. 41–48.

[75] Taylor, G. I., 1934, "The Formation of Emulsions in Definable Fields of Flow," Proc. R. Soc. London, Ser. A, 146(858), pp. 501–523.

[76] Shapira, M., and Haber, S., 1990, "Low Reynolds Number Motion of a Droplet in Shear Flow Including Wall Effects," Int. J. Multiphase Flow, 16(2), pp. 305–321.

[77] Zhou, H., and Pozrikidis, C., 1993, "The Flow of Suspensions in Channels: Single Files of Drops," Phys. Fluids, 5(2), pp. 311–324.

[78] Tang, H., Wrobel, L., and Fan, Z., 2004, "Tracking of Immiscible Interfaces in Multiple-Material Mixing Processes," Comput. Mater. Sci., 29(1), pp. 103–118.

[79] Soligo, G., Roccon, A., and Soldati, A., 2020, "Deformation of Clean and Surfactant-Laden Droplets in Shear Flow," Meccanica, 55, pp. 371–386.

[80] Sander, W., and Weigand, B., 2008, "Direct Numerical Simulation and Analysis of Instability Enhancing Parameters in Liquid Sheets at Moderate Reynolds Numbers," Phys. Fluids, 20, p. 053301.

[81] Kozul, M., Costa, P. S., Dawson, J. R., and Brandt, L., 2020, "Aerodynamically Driven Rupture of a Liquid Film by Turbulent Shear Flow," Phys. Rev. Fluids, 5, p. 124302.

[82] Lasheras, J., Eastwood, C., Mart Inez-Bazán, C., and Montanes, J., 2002, "A Review of Statistical Models for the Break-Up of an Immiscible Fluid Immersed Into a Fully Developed Turbulent Flow," Int. J. Multiphase Flow, 28(2), pp. 247–278.

[83] Eastwood, C. D., Armi, L., and Lasheras, J., 2004, "The Breakup of Immiscible Fluids in Turbulent Flows," J. Fluid Mech., 502, pp. 309–333.

[84] Ruiz-Rus, J., Ern, P., Roig, V., and Martínez-Bazán, C., 2022, "Coalescence of Bubbles in a High Reynolds Number Confined Swarm," J. Fluid Mech., 944, p. A13.

[85] Håkansson, A., and Brandt, L., 2022, "Deformation and Initial Breakup Morphology of Viscous Emulsion Drops in Isotropic Homogeneous Turbulence With Relevance for Emulsification Devices," Chem. Eng. Sci., 253, p. 117599.

[86] Olad, P., Innings, F., Crialesi-Esposito, M., Brandt, L., and Håkansson, A., 2023, "Comparison of Turbulent Drop Breakup in an Emulsification Device and Homogeneous Isotropic Turbulence: Insights From Numerical Experiments," Colloids Surf., A, 657, p. 130569.

[87] Farsoiya, P. K., Liu, Z., Daiss, A., Fox, R. O., and Deike, L., 2023, "Role of Viscosity in Turbulent Drop Break-Up," J. Fluid Mech., 972, p. A11.

[88] Kolmogorov, A. N., 1991, "The Local Structure of Turbulence in Incompressible Viscous Fluid for Very Large Reynolds Numbers," Proc. R. Soc. London, Ser. A, 434(1890), pp. 9–13.

[89] Hinze, J., 1955, "Fundamentals of the Hydrodynamic Mechanism of Splitting in Dispersion Processes," AIChE J., 1(3), pp. 289–295.

[90] Perlekar, P., Biferale, L., and Sbragaglia, M., 2012, "Droplet Size Distribution in Homogeneous Isotropic Turbulence," Phys. Fluids, 24(6), p. 065101.

[91] Vela-Martín, A., and Avila, M., 2022, "Memoryless Drop Breakup in Turbulence," Sci. Adv., 8(50), p. eabp9561.

[92] Garrett, C., Li, M., and Farmer, D., 2000, "The Connection Between Bubble Size Spectra and Energy Dissipation Rates in the Upper Ocean," J. Phys. Oceanogr., 30(9), pp. 2163–2171.

[93] Deane, G. B., and Stokes, M. D., 2002, "Scale Dependence of Bubble Creation Mechanisms in Breaking Waves," Nature, 418, p. 839.

[94] Deike, L., Melville, W., and Popinet, S., 2016, "Air Entrainment and Bubble Statistics in Breaking Waves," J. Fluid Mech., 801, pp. 91–129.